Kinetic Study of Gas-Phase Reactions of Pyruvic Acid with HO_2

Jonathan R. Church, Veronica Vaida and Rex T. Skodje*

Department of Chemistry, University of Colorado, Boulder, CO 80309-0215

Abstract

Gas-phase reactions between pyruvic acid (PA) and HO_2 radicals were examined using *ab initio* quantum chemistry and transition state theory. The rate coefficients were determined over a temperature range of 200 to 400K including tunneling contributions. Six potential reaction pathways were identified. The two hydrogen abstraction reactions yielding the H_2O_2 product were found to have high barriers. The HO_2 radical was also found to have a catalytic effect on the intramolecular hydrogen transfer reactions occurring by three distinct routes. These hydrogen-shift reactions are very interesting mechanistically although they are highly endothermic. The only reaction which contributes significantly to the consumption of PA is a multistep pathway involving a peroxy-radical intermediate, $PA+HO_2 \rightarrow CH_3COOH+OH+CO_2$. This exothermic process has potential atmospheric relevance because it produces an OH radical as a product. Atmospheric models currently have difficulty predicting accurate OH concentrations for certain atmospheric conditions, such as environments free of NOx and the nocturnal boundary layer. Reactions of this sort, although not necessary with PA, may account for a portion of this deficit. The present study helps settle the issue of the relative roles of reaction and photolysis in consumption of PA in the troposphere.

* *Corresponding author:* rex.skodje@colorado.edu

1. Introduction

Atmospheric chemistry is largely driven by reactive radical species, notably HOx (OH + HO_2). The hydroxyl radical OH is the strongest oxidizing agent in the Earth's atmosphere. Reactions of OH with volatile organic compounds[1 2 3 4 5 6] (VOC) are important and while HO_2 is less reactive it is often present in much higher concentrations than is OH. Given the importance of these radicals in atmospheric chemistry, their sources, sinks and interconversions in different environments is of utmost interest and is studied by field measurements, laboratory studies and atmospheric models.[3 6] It is known that in urban polluted environments with high NO_X (NO + NO_2) and VOC content, low ratios of HO_2 to OH and therefore high OH mixing ratios maintain a high oxidative capacity and the ability to remove VOCs in these polluted environments. However,

in pristine environments above the tropical forests where large biogenic emissions such as isoprene are found and also at nighttime in the boundary layer the HO_2 to OH ratio is high (100:1). In these environments HO_2 is well modeled however large OH sources are missing.[7 8 9 10 11 12] Interestingly, it has been shown that the autoxidation of peroxy radicals may have important atmospheric implications.[13 14 15 16] In response to the OH deficit found within certain atmospheric models, da Silva proposed a new class of reactions focused on the conversion of HO_2 to OH which involved the autoxidation of peroxy radicals.[7] The new mechanisms proposed involve the oxidation of glyoxal and several other OVOCs by HO_2 leading to OH as well as carboxylic acids, compounds currently underrepresented in atmospheric models.[17] In this work we consider and compare different pathways by which HO_2 oxidizes pyruvic acid including an interesting analog of the da Silva mechanism.[7]

We explore the reactions of HO_2 with the pyruvic acid (PA) molecule, $CH_3(CO)COOH$, using theoretical methods, noting that experimental rates are not available. The motivation is twofold: first to assess the question of the importance of chemical processing of atmospheric PA relative to photolysis, and second to investigate the PA+HO_2 reactions mechanistically to probe whether HO_2 to OH conversion may be possible via this route. Pyruvic acid is a keto-acid prevalent in the Earth's atmosphere[18 19 20 21 22 23 24 25] in gas phase, and also is found in atmospheric aerosol, fogs, clouds and polar ice. In regions with abundant vegetation, it can be emitted directly by plants, yet its main source is the oxidation of isoprene, ozonolysis of methylvinylketone and the subsequent hydrolysis of the Criegee intermediate formed. It can also be formed in the photolysis of methylglyoxal generated from the reaction of biogenic VOCs including monoterpenes and has been detected in biomass burning plumes. In the atmosphere, it is believed that the primarily loss mechanism of PA is due to photolysis.[26 27 28 29] The primary photolysis products are acetaldehyde and CO_2 and the photolysis rates have been well studied.[30 31 32 33 34 35 36 37 38 39 40 41 42 43 44 45 46 47 48 49 50] In competition with photochemical loss of PA, are the oxidation reactions, especially by radical species such as OH and HO_2. The reaction rate with OH has been experimentally estimated to be slow, although only one observation has been reported.[51] We have recently constructed a theoretical model of the OH+PA system using *ab initio* transition state theory.[52] That study revealed the primary reactive process was hydrogen abstraction to form water and either $CH_2(CO)COOH$ or CH_3CO+CO_2 products. While a variety of interesting features were revealed in that study, it was also concluded that the overall rate of OH+PA was slow for

atmospheric temperatures. The loss of PA by OH oxidation was not competitive with that of photolysis and experimental estimates by Reed Harris *et al.* suggest that loss through OH oxidation was up to two orders of magnitude slower than that of photolysis.[43] It is reasonable to next consider the reactions of PA with HO_2 since no measurements are available at present in the literature and suggestions that oxidation by HO_2 in organic compounds could be competitive.

Another reason to investigate PA + HO_2 is the interesting mechanistic character of HO_2 reactions. In previous works it had been discovered that HO_2 can catalyze intramolecular H-atom transfer reactions through a concerted double H-atom transfer mechanism. For reactions as simple as $DX+HO_2 \rightarrow HX+DO_2$ (X=F, Cl, Br, I)[53 54] the process is operative. Karton[55] studied the HO_2 catalyzed tautomerization of vinyl alcohol that operates via a similar mechanism. For the PA case, we can imagine an H-atom transferred from the acid group to the ketone oxygen (i.e. $CH_3(CO)COOH \rightarrow CH_3COH(CO)O$ which is quickly followed by decarboxylation to yield the carbene product CH_3COH.[48 49 50] This decarboxylation reaction was previously studied by Takahashi *et al.*[41] as a unimolecular process activated by high overtone excitation. It will be interesting to see if the reaction barrier can be lowered using the concerted double H-atom exchange process mediated by HO_2. Overall, it is found that $PA+HO_2$ can proceed to several different products. Direct abstraction from the methyl site or acid site can yield the two respective channels

$$CH_3(CO)COOH + HO_2 \rightarrow CH_2(CO)COOH+H_2O_2 \quad \text{R1}$$

$$CH_3(CO)COOH + HO_2 \rightarrow CH_3CO+CO_2+H_2O_2 \quad \text{R2}$$

The HO_2 mediated H-atom transfer mechanism can produce

$$CH_3(CO)COOH + HO_2 \rightarrow CH_2COH(CO)OH+HO_2 \quad \text{R3}$$

$$CH_3(CO)COOH + HO_2 \rightarrow CH_3COH(CO)O+HO_2 \quad \text{R4}$$

$$CH_3(CO)COOH + HO_2 \rightarrow CH_3COH+CO_2+HO_2 \quad \text{R5}$$

A final process can produce acetic acid and OH, i.e.

$$CH_3(CO)COOH + HO_2 \rightarrow CH_3COOH+CO_2+OH. \quad \text{R6}$$

This later process is quite interesting in that it converts the relatively stable radical HO_2, into the much more reactive species OH. It is also a potential source for the missing OH content in the atmosphere via a mechanism quite analogous to that suggested by da Silva for methylglyoxyl.[7]

In Sec. 2, we present the computation methods used in this work. The rate coefficients are obtained using tunneling corrected transition state theory. The role of conformational structures of the reactants and of the transition state are explicitly included. The quantum chemistry calculations are carried out using the M11 density functional for structures and frequencies and CCSD(T) theory energetics. In Sec. 3.1 the structures and mechanism are presented and discussed. The rate coefficients are presented in Sec. 3.2 including a discussion of the role of conformations and of tunneling. Finally, in Sec. 4 a brief conclusion is presented. Furthermore, in the Supporting Information we present the detailed results of the quantum chemistry calculations.

2. Computational Methods

The rate coefficients were computed using transition state theory (TST) where the parameters were established using *ab initio* quantum mechanics (QM). In the conventional form of TST, bimolecular reactions that proceed along a single reaction pathway from a single well-defined reactant structure have a rate coefficient as defined as

$$k^{TST}(T) = \frac{k_B T}{h}\kappa(T)\frac{Q^{\ddagger}}{\mathrm{Q_A}\cdot\mathrm{Q_B}}\,\mathrm{e}^{-\frac{\Delta E_0^{\ddagger}}{k_B T}} \qquad (1)$$

The transition state which acts as the bottleneck is the highest saddlepoint along the reaction pathway between reactants and products and $\Delta E_0^{\ddagger}$ denotes the zero-point corrected barrier height relative to the ground state of the reactants. Quantum mechanical tunneling is incorporated through the transmission coefficient κ(T). The canonical partitions functions per unit volume of the reactants and saddlepoints, Q_A, Q_B, and $Q^{\ddagger}$ were calculated using the harmonic oscillator-rigid rotor (HO-RR) approximation using the parameters at the stationary points of the potential and $\Delta E_0^{\ddagger}$ is taken as the barrier between the zero-point corrected reactants and transition state.

In the case of the reaction of HO_2 with PA, the situation is more complicated since the reactants have multiple conformational structures resulting from orientations along two relevant torsional degrees of freedom. Furthermore, there are several saddlepoints corresponding to different conformations of the {$HO_2\cdots$PA} complex and various possible reaction paths going to

different products. The generalization of the conventional TST formalism to such circumstances has been object of considerable interest recently. Here we shall employ a simple version of the multipath TST (MPTST) introduced by Truhlar and coworkers which we briefly describe in the context of PA+HO_2.[56] This expression is similar to one which has been used by Vereecken and Peteers for studying rotamers.[57]

The PA molecule has four conformational structures shown in Fig. 1, which are annotated with the zero-point corrected energies. These conformers correspond to cis-trans structures along the torsions about the alcohol C-OH and C-C bonds, respectively. Of the four structures, however, only two major conformers are important in the gas-phase chemistry of the molecule under ambient conditions. These are the Trans-cis (Tc) conformer which contains an intramolecular hydrogen bond between the carboxylic acid and ketone functional groups and the Trans-trans (Tt) conformer where the hydrogen of the carboxylic acid is trans relative to the ketone oxygen.

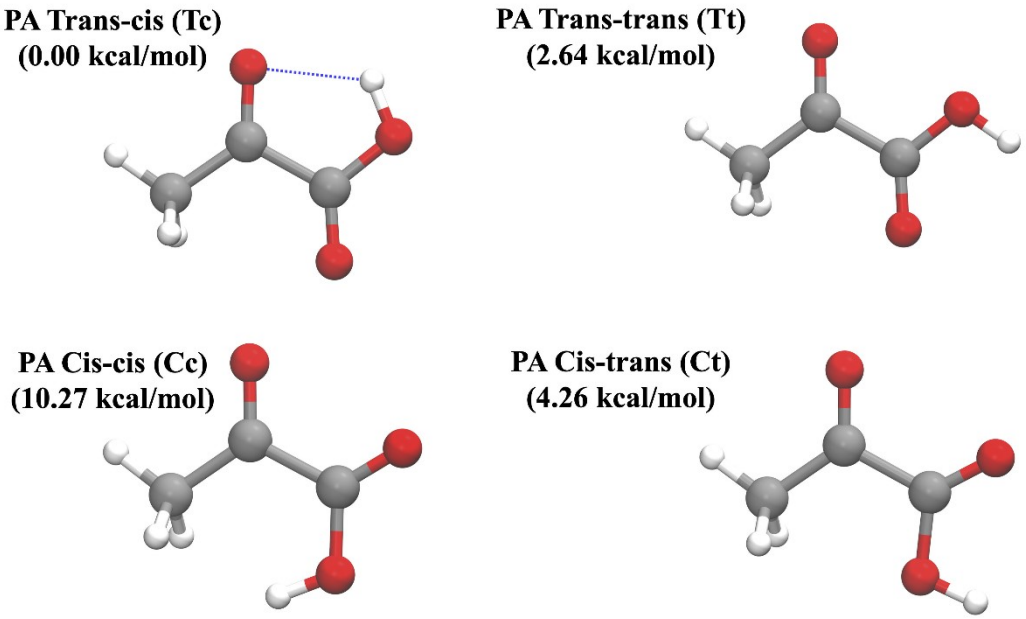

Figure 1. Stationary point structures for the Trans-cis (Tc), Trans-trans (Tt), Cis-trans(Ct) and Cis-Cis (Cc) conformers of pyruvic acid, as well as their respective energies relative to Tc calculated using CCSD(T)/CBS in tandem with structures obtained using M11/cc-pVTZ. Here a blue line indicates an intramolecular hydrogen bond, which is responsible for the additional stability in the PA(Tc) conformer.

PA(Tc) is the more thermally abundant conformer of those found in the gas-phase due to the stabilization provided by the intra-molecular hydrogen bond which lowers the energy by ε=2.64

kcal/mol when compared to PA(Tt).[31 39 41] The total partition function of PA is then the weighted sum of contributions from PA(Tc) and PA(Tt)

$$Q_{PA} = Q_{Tc} + \exp\left(-\frac{\varepsilon}{k_B T}\right) Q_{Tt} \tag{2}$$

where contributions from each conformer are then computed using the HO-RR approximation for all modes. This form is simpler than the multi-structural expression of Truhlar and coworkers in that the torsional anharmonicity is ignored. [56]

The various transition state structures (i.e. saddlepoints) can be grouped into sets of conformational isomers that proceed to the same chemical products, based on knowledge of the reaction paths. These structures will be discussed in detail in the next section. Each of these saddlepoints will possess a distinct barrier height and will have a distinct tunneling coefficient. Hence, the generalization of eq. (1) will involve a summation over the contributions of each barrier. [58 59] Thus, a given reaction R_i has M_i distinct TS-conformational structures, labeled by j, so that its TS is labeled by the pair (i,j). The rate coefficient for the reaction R_i is

$$k_i(T) = \frac{k_B T}{h} \frac{\sum_j^{M_i} \kappa_{i,j}(T)\, Q_{i,j}^{\ddagger} \exp\left(-\frac{\Delta E_{0;\,i,j}^{\ddagger}}{k_B T}\right)}{Q_{PA} \cdot Q_{HO_2}} \tag{3}$$

In eq. (3), the barrier energy $\Delta E_{0;\,i,j}^{\ddagger}$ is computed relative to the lowest energy conformer of the reactants, i.e. PA(Tc)+HO_2. Each of the terms $Q_{i,j}^{\ddagger}$ is a HO-RR partition function associated with the saddlepoint (i,j), where one vibrational degree of freedom is eliminated, i.e. the reaction coordinate. The tunneling coefficients will, in general, be different for each saddlepoint structure. This formula can be regrouped in various equivalent ways, e.g. by factoring out the lowest barrier from the exponential term. This expression presumes that the conformers of the TS are in thermal equilibrium with the reactants and that all the conformers of the reactants are in a thermal equilibrium with the bath. We assume that this approximation holds in the present problem. The calculation of the tunneling coefficients is accomplished using the Small Curvature Tunneling method (SCT).[60] The SCT method is an improved technique based on the earlier SC-SAG concept[61 62] that incorporates corner cutting tunneling dynamics based on a local analysis of the reaction pathway. The method is known to produce accurate results for a variety of multidimensional reactive systems.

The geometry optimizations of the reactants and saddlepoints were carried out using the using the M11 functional with the cc-pVTZ basis. The vibrational frequencies were then scaled with a factor of 0.967. The stationary point energetics of the transition states were carried out at a higher level using CCSD(T). The reported values of the energies were obtained by extrapolation to the CBS limit using ROCCSD(T)/cc-pVXZ(X=D,T,Q) and M11/cc-pVXZ(X=D,T,Q).[63] [64]The vibrational frequencies and structures obtained using M11/cc-pVTZ as well as the single point energetics and the respective CBS extrapolated energy can be found within the supplementary information. To obtain the minimum energy path (MEP), we employed the GS2 algorithm which permits a fairly large step size during integration while still yielding accurate results.[65] [66] [67] [68] [69] The method is also quite good at handling the stiffness problem frequently encountered when solving for an IRC.[68] The geometry optimizations, frequency calculations and all subsequent M11 functional calculations were performed using the GAMESS-US computational package[70]. CCSD(T) calculations were carried out using the GAUSSIAN 16 software package.[71]

3. Results and Discussion

3.1 Structures and Mechanisms

The stationary points for the PA + HO_2 system were located using the quadratic approximation search algorithm found within GAMESS-US. Many of the structures were conformational isomers of one another or mirror image structures that we combine in the kinetic analysis. We located four stable points, that we classify as pre-reactive complexes of PA-HO_2, 16 separate saddlepoints for the reactive steps, and 10 intermediates corresponding to various metastable structures along various reaction pathways. We first discuss the pre-reactive complexes and then move on to analyze the reaction mechanism via the saddles and reactive intermediates.

Four hydrogen bound pre-reactive complex structures involving HO_2 and pyruvic acid were found and are presented in Fig. 2.

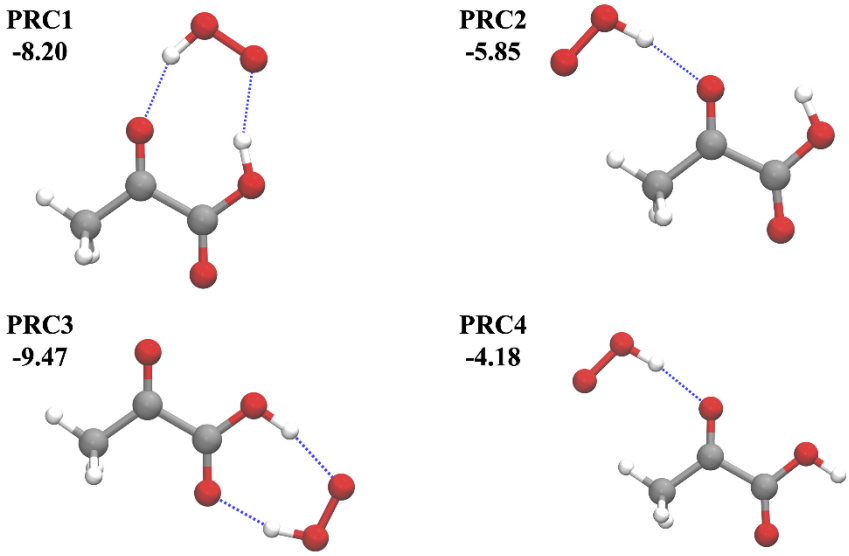

Figure 2. Hydrogen bound pre-reactive complex (PRC) structures optimized using M11/cc-pVTZ for the PA + HO_2 reaction. Additionally, the M11/CBS energetics relative to the PA(Tc)+HO_2 are given in kcal/mol. Blue lines indicate hydrogen bonds formed during complex formation.

The first and third pre-reactive complex structures (PRC1 and PRC3) are formed through hydrogen bond interactions between the carboxylic acid of pyruvic acid and the ketone oxygen. The second and fourth complexes (PRC2 and PRC4) are formed through hydrogen bond interactions with the methyl functional group and ketone oxygen and are conformers of each other. The M11/CBS zero-point corrected internal energies for these complexes relative to asymptotic reactants of PA(Tc) and HO_2 are presented in Table 1 (since these energies do not affect the rate calculations, we do not improve them to the CCSD(T) level). The complexes formed through interactions with the acid functional group (PRC1 and PRC3) were found to be more energetically favorable than those formed through interactions with the methyl group due to the double hydrogen bonds. PRC3 is more stable than PRC1 due to the decreased ring strain in the structure. On the other hand, PRC4 was found to be less stable than PRC2 because of the missing additional intramolecular hydrogen bond found in the Tc conformation of the complex. While the PRC's are interesting, they do not play a role in the kinetic rates in the high-pressure limit due to being in thermal equilibrium with the bimolecular reactants. However, the PRC's help characterize the geometries and energetics associated with hydrogen bonding within the PA-HO_2 collision complex. The intermolecular hydrogen bond between HO_2 and PA is roughly 4-5 kcal/mol/bond compared with 2.64 kcal/mol for the intramolecular hydrogen bonding. It will be interesting to compare the strength of the analogous hydrogen bonding in the transition state region.

Table 1. Zero-point energy corrected energies for the pre-reactive complexes (PRC), reaction intermediates (INT) and reaction products (P1-P6 for reactions R1-R6) of the various PA+HO_2 pathways relative to PA(Tc)+HO_2 expressed as kcal/mol. The energies were calculated using M11/CBS singlepoint energies and the frequencies determined with M11/cc-pVTZ. Because the rate coefficients are calculated at the high-pressure limit, these structures do not play a role in the rate constants and were therefore not improved to the CCSD(T) level.

	ΔE_{CBS}^{M11}
PRC1	-8.20
PRC2	-5.85
PRC3	-9.47
PRC4	-4.18
INT1+HO_2	10.69
INT2+HO_2	16.22
INT3	29.04
INT4	21.76
INT5	16.82
INT6	-9.22
INT7	-6.67
INT8	-7.60
INT9	-15.91
INT10	-12.88
P1+H_2O_2	9.35
P2+H_2O_2+CO_2	-6.54
P3/P4+HO_2+CO_2	41.54
P5+HO_2	28.38
P6+OH+CO_2	-64.61

The overall heats of reaction determined using M11/CBS for the products of reactions R1-R6 are listed in Table 1 as PX(X=1-6). It is seen that the reaction is exothermic only for reactions R2 and R6. The isomerization reactions R3, R4, and R5 as well as the abstraction process R1 were all found to be endothermic. Presumably, the reactions R2 and R6 would be the only available avenues for reaction under ambient conditions.

The energetics of the stationary points of reactions R1-R5 are shown in Fig. 3 and that of reaction R6 is given in Fig. 4. The numerical results from both CCSD(T)/CBS and M11/CBS are tabulated in Table 2 for the transition states. The optimized TS structures of R1-R5 are shown in Fig. 5 and those of R6 in Fig. 6. The structures of the intermediates along the pathways are given in Fig. 7 and 8, respectively. The abstraction and exchange reactions (R1-R5) were found to have

extremely high adiabatic (zero point corrected) barriers ranging from 15.05 kcal/mol to 32.81 kcal/mol at the CCSD(T)/CBS level of theory. In contrast, the primary bottleneck of R6 has a much lower barrier, 7.29 kcal/mol, which motivates singling it out from the other processes. We next describe some of the mechanistic aspects of these six reaction motifs.

Table 2. Zero-point corrected energetics for the reactions of PA+HO_2 calculated using both CCSD(T)/CBS and M11/CBS in kcal/mol relative PA(Tc) + HO_2. Here $\Delta E_{TS}^{CCSD(T)}$ corresponds to the CCSD(T)/CBS adiabatic barrier determined using M11/cc-pVTZ structures and frequencies, and ΔE_{TS}^{M11} corresponds to the barriers determined using the same structure and frequencies with M11/CBS. Also presented are the barrier frequencies of each saddlepoint in cm^{-1}.

	$\Delta E_{TS}^{CCSD(T)}$	ΔE_{TS}^{M11}	$\nu^{\ddagger}$
TS1	19.17	20.98	2334.24*i*
TS2	30.20	27.91	4896.87*i*
TS3	25.81	22.76	1556.98*i*
TS4	32.81	25.98	1110.95*i*
TS5	31.95	30.62	210.40*i*
TS6	15.05	16.93	174.68*i*
TS7	-0.09	2.32	832.42*i*
TS8	-1.01	1.88	925.78*i*
TS9	1.97	1.89	804.85*i*
TS10	6.01	8.95	853.32*i*
TS11	-8.54	-6.20	114.68*i*
TS12	1.26	2.95	600.42*i*
TS13	7.29	7.39	1375.96*i*
TS14	13.26	12.25	2245.75*i*
TS15	-12.69	-12.94	583.06*i*
TS16	-8.68	-8.84	326.75*i*

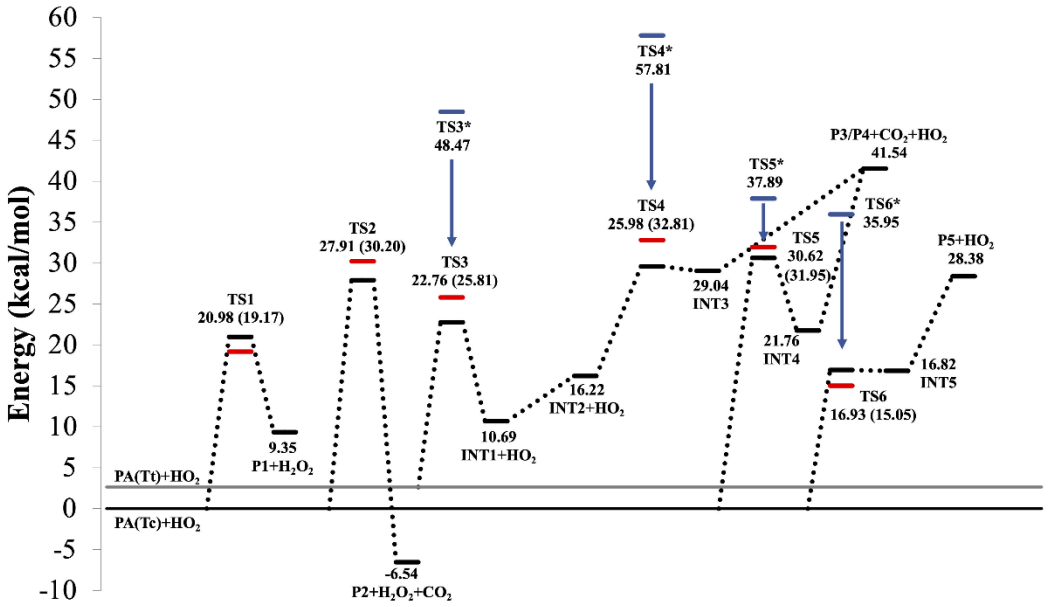

Figure 3. Schematic for the zero-point corrected single point energies for the reactions originating from PA(Tc) and PA(Tt) with HO_2. The energies presented are relative to PA(Tc). The energetics of both the minima and saddlepoints structures were calculated using M11/CBS (Black) in kcal/mol with the M11/cc-pVTZ structures and frequencies. Additionally, the transition state (TSx) energetics were also calculated using CCSD(T)/CBS (Red) using the DFT structures and frequencies. Numerical values outside of parentheses correspond to DFT energetics and inside correspond to CCSD(T) energetics. The values of several unimolecular barriers calculated using M11/CBS are presented in blue (TS3*, TS4*, TS5* and TS6*) in order to demonstrate the catalytic effect HO_2 can have on the unimolecular barriers for intramolecular hydrogen transfer.

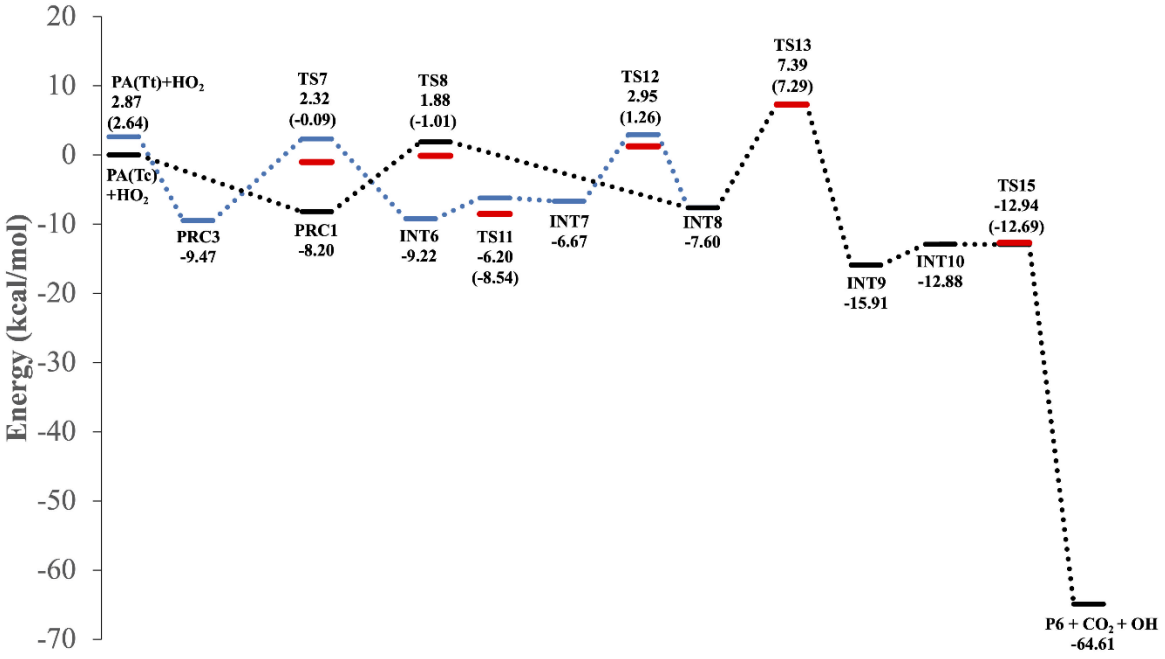

Figure 4. Lowest energy structures for the R6 reaction pathway of PA+HO_2. M11/CBS energies corresponding to the PA(Tc) are in black, and those corresponding to PA(Tt) are in blue. The energies presented are relative to PA(Tc). CCSD(T)/CBS (Red) was also used to calculate the adiabatic barriers of each transition state (TSx) for both the Tc and Tt conformer pathways using the structures and frequencies calculated using M11/cc-pVTZ.

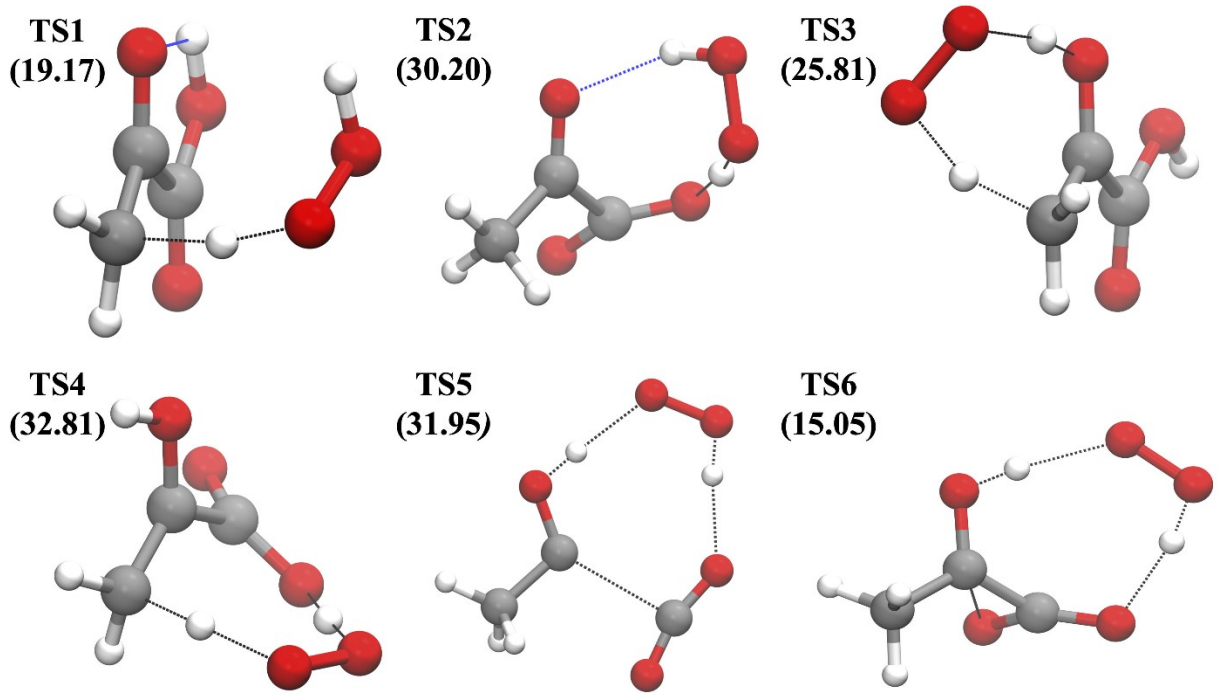

Figure 5. Transition state structures for reactions R1-R5 optimized using M11/cc-pVTZ for the PA + HO_2 reactions. TS1, TS2, TS5, and TS6 resemble PA(Tc) and TS3, TS4, resemble PA(Tt). CCSD(T)/CBS energetics relative to PA(Tc)+HO_2 are presented in parenthesis. Here black lines indicate bonds breaking and forming and blue lines indicate hydrogen bonds.

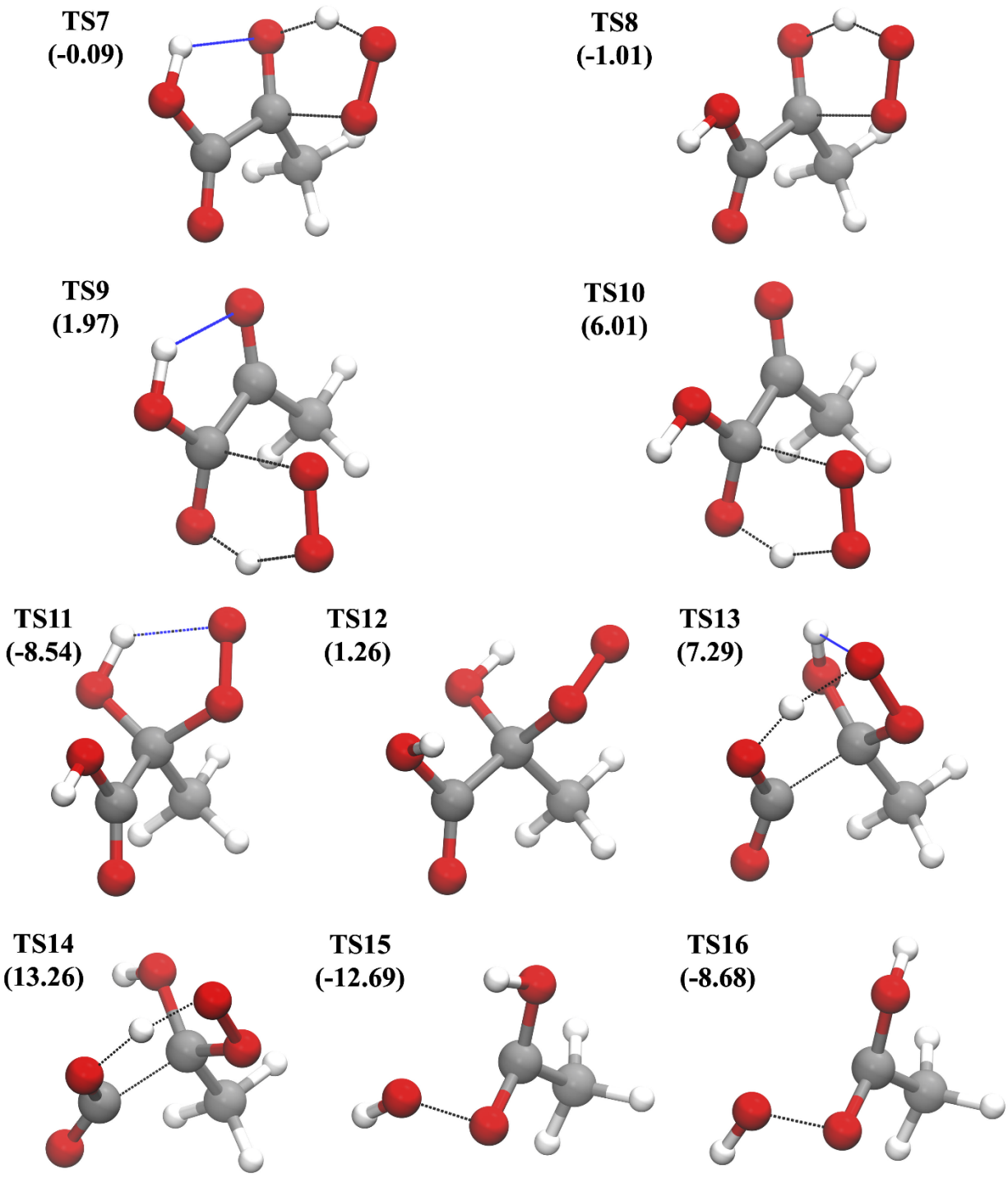

Figure 6. Transition state structures involved in the reaction pathway R6 optimized using M11/cc-pVTZ. CCSD(T)/CBS energetics relative to PA(Tc)+HO_2 are presented in parenthesis. Here black lines indicate bonds breaking and forming and blue lines indicate hydrogen bonds. The saddlepoints TS7 and TS8 lead to a peroxy formation through the ketone carbon from the PA(Tc) and PA(Tt) conformers respectively and TS9 and TS10 structures lead to a peroxy radical formed from an addition to the carboxylic acid carbon. The conformational pairs for TS7/TS8, TS13/14,

and TS15/TS16 involve the orientation of the OH-group and thus affect the degree of hydrogen bonding.

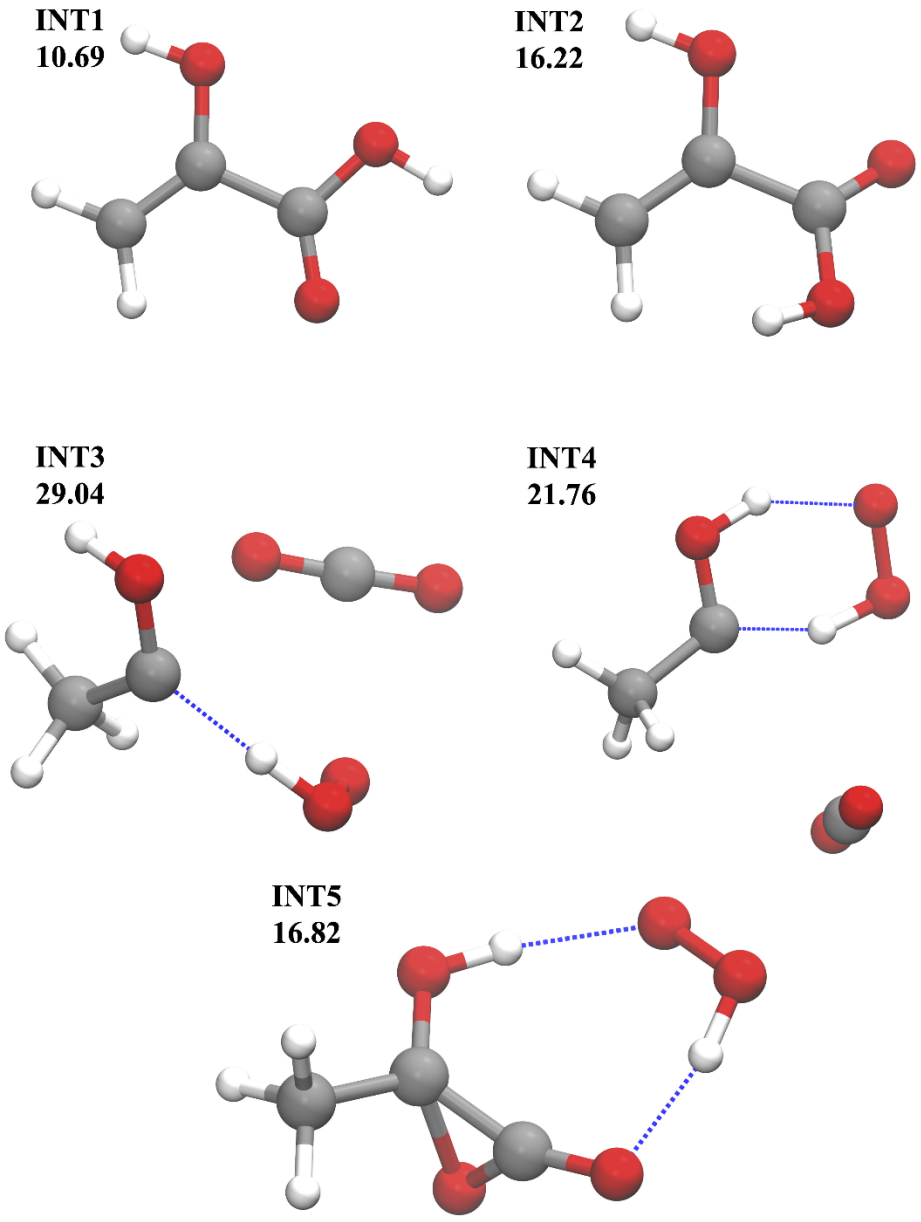

Figure 7. Intermediate (INT) metastable structures found along the R1 to R5 reaction pathways calculated using M11/cc-pVTZ. M11/CBS energetics relative to PA(Tc)+HO_2 are presented.

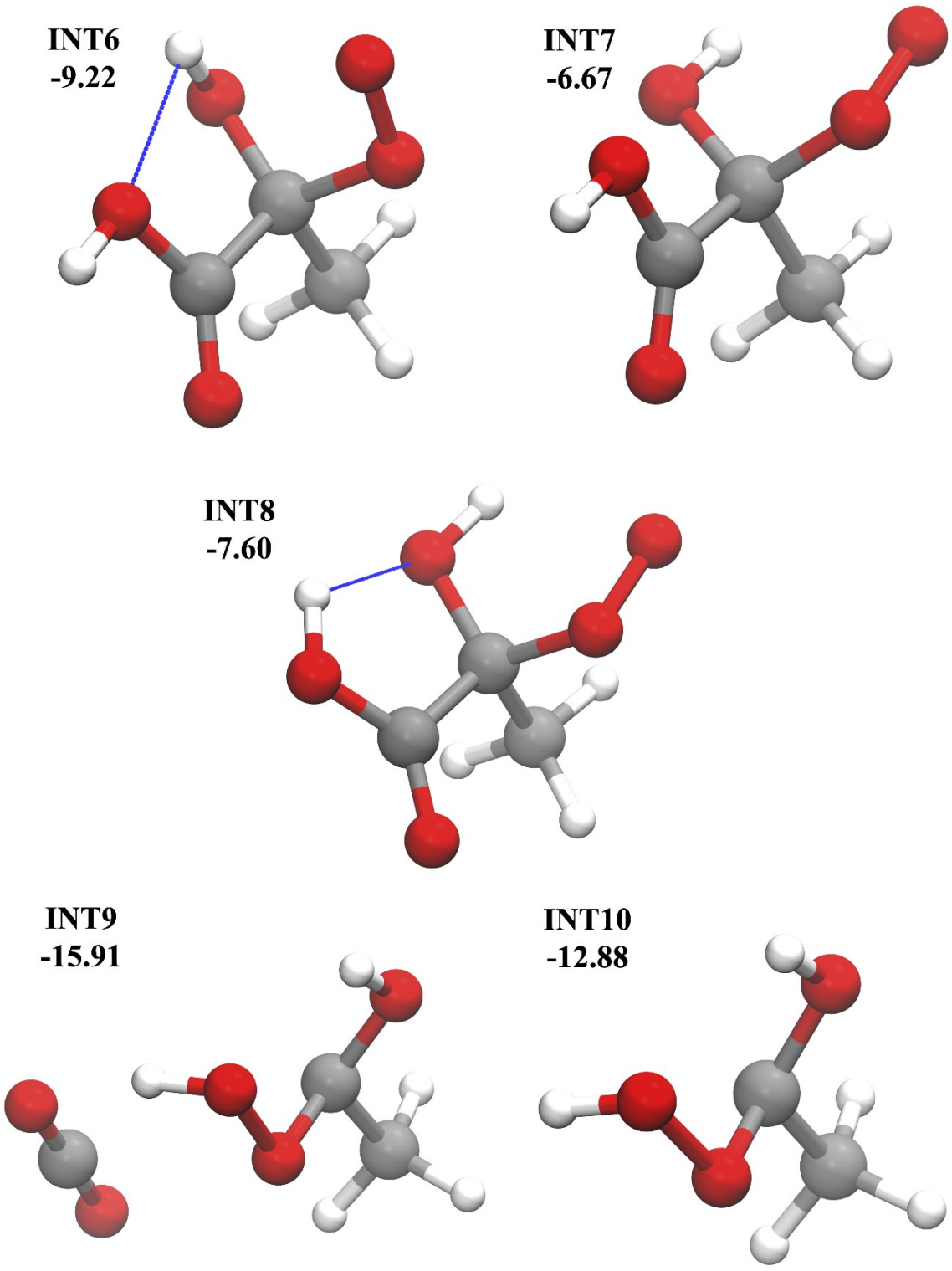

Figure 8. Intermediate metastable structures for the R6 reaction leading to the formation of $CH_3COOH+OH+CO_2$ computed with M11/cc-pVTZ. The intermediates INT6, INT7 and INT8 are associated with changes in the orientation of the two OH-groups.

Consider first the reactions R1 and R2 which are abstraction type processes yielding an H_2O_2 product. In R1, the H-atom is abstracted from the methyl group while in R2 the acid group H-atom is abstracted. The R1 abstraction takes place through TS1 with a barrier of 19.17 kcal/mol at the CCSD(T)/CBS level. The product is then simply the methyl site radical species $CH_2(CO)COOH$. The acid group H-atom abstraction, via TS2, has an even higher barrier of 30.20 kcal/mol. Since the resulting $CH_3(CO)(CO)O$ complex is unstable it immediately decarboxylates to form an acetyl radical along with CO_2 and H_2O_2. These reactions are simple single atom transfer processes, but even the reactions with large transmission coefficients yield small rate constants at each temperature studied because of their high reaction barriers.

Reaction R3-R5 are HO_2 mediated H-transfer reactions where the H-atom migrates to a new site on the PA molecule via a double exchange process with HO_2. The HO_2 catalyst is known to significantly lower the barrier for these sorts of unimolecular reactions.[54 55] In R3 the H-atom is transferred from the methyl group to the ketone oxygen. Reaction R3 proceeds via a two-step isomerization process which ultimately lead to methylhydroxycarbene, which is the same product produced from the direct gas-phase photolysis of the pyruvic acid molecule.[41 50 38] In R3, a transient radical $CH_2COHCOOH$ is formed as an intermediate product species. If we allow this radical to further decompose it forms the products $CH_3COH+CO_2$. These reactions proceed through ring shaped TS's as shown in Fig. 5. However, the overall reaction energetics is highly endothermic, ΔH_{rxn}=41.54 kcal/mol indicating that none of these structures is the rate limiting bottleneck. Nevertheless, it is interesting to note that HO_2 dramatically lowers the saddlepoint energies compared to the uncatalyzed reactions which are relevant to the overtone induced reaction of the bare PA molecule. The comparison is shown on Fig. 3 where the analogous unimolecular energy, TS3*, is indicated. In reaction R4 and R5, the HO_2 species catalyzes the H-atom migration from the acid group to the ketone. The unstable $CH_3COHCOO$ transient, either forms a lactone product in R5, or dissociates to the $CH_3COH+CO_2$ product. Again, the overall reactions are highly endothermic and unimportant in the kinetics at ambient temperatures.

Table 3. Energies (kcal/mol) of the transition state relative to reagents for the $PA+HO_2$ catalyzed reaction versus uncatalyzed unimolecular reaction. The zero point corrected single surface results of da Silva[42] (a) and Takahashi (b) *et al*[41] are shown along with the heat of reaction. Note the catalyzed barriers are all submerged relative to the final products.

	ΔE_{TS}^{Cat}	ΔE_{TS}^{uni}	ΔH_{rxn}
R3[b]	32.81	60.00	43.00
R4[b]	31.95	38.28	40.63
R5[a]	15.05	35.60	28.70

The lowest energy reaction pathway for PA+HO_2 is found to be reaction R6. This highly exothermic reaction consists of two sequential H-atom transfer reactions. It is analogous to the reactions of HO_2 with methylglyoxal studied by da Silva which acts as a pathway for OH radical formation.[7] The structures arranged along the pathway are depicted in Fig. 9 where we have distinguished PA(Tc) and PA(Tt) for clarity. In the first step, the HO_2 attacks the central carbon and transfers an H-atom to the ketone oxygen passing over the transition states TS7 or TS8. As seen in Fig. 9, these two transition states are conformational isomers associated with the orientation of the OH-group on the carboxylic acid with TS7 similar to PA(Tc) and TS8 similar to PA(Tt). TS7 is slightly lower in energy compared with TS8 due to additional intramolecular hydrogen bonding. The intermediate structures INT6 and INT8 are the products of these two reaction steps, and correspond to conformations of the OH-orientation. It is possible for the intermediates INT6 and INT8 to interconvert by passing over either of two low lying transition state, TS11 and TS12, that link the two pathways. Both of these additional saddlepoint structures, TS11 and TS12, connecting INT6 and INT8 correspond to conformational changes of the acid and central alcohol hydrogen respectively. We note that INT6 and INT8 are relatively stable intermediates, lying 7.60 and 9.22 kcal/mol below the entrance channel asymptote for PA(Tc)+HO_2.We assume, consistent with eq. 3, that INT6 and INT8 are populated in thermal equilibrium.

The key bottleneck step in the reaction of PA with HO_2 is the second H-atom transfer process that proceeds through either of the conformational pair TS13 or TS14. This step consists of a concerted hydrogen transfer from the acid OH to the peroxy simultaneously with the decarboxylation of the CO_2 group. This rate limiting step is then followed by OH removal through either TS12[a] or TS12[b]. The barriers for TS13 and TS14, of 7.29 and 13.26 kcal/mol are the highest along the pathway, and thus we can assume that everything on the reactant side of these barriers are in thermal equilibrium. The difference in energy between these two saddlepoint structures is large enough such that it is unlikely that TS14 will contribute in the TST computation of the rate.

It is worth noting that the energy of TS13 is much lower that limiting barriers for any of the competing reaction R1-R5, suggesting that R6 should dominate the kinetics.

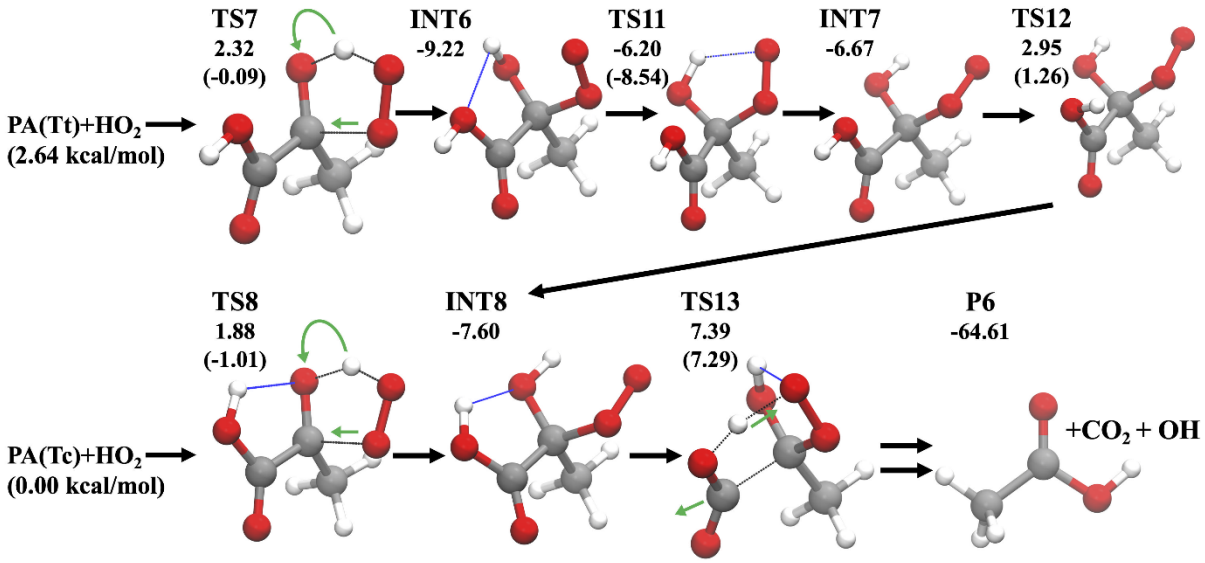

Figure 9. The scheme for reaction R6, $PA+HO_2 \rightarrow CH_3(CO)OH+CO_2+OH$. The interconversion between conformers INT7 and INT8 is shown. The TS13 is rate determining. The blue arrows provide a sense of atomic movement in given reaction steps. M11/CBS energetics relative to the $PA(Tc)+HO_2$ are presented and CCSD(T)/CBS energetics are presented for saddlepoints in parenthesis.

3.2 Determination of the Rate Coefficient

Having characterized the transition states for the reactions of HO_2 with PA, we can now compute the rate coefficients. Since reactions R3, R4, and R5 are dominated by extremely high reaction endothermicity, we shall omit computation of those very small rates. For the remaining reactions R1, R2, and R6 studied we apply eq. (3) in the range 200-400K. The structures and frequencies were obtained with the M11 functional while the energetics employed CCSD(T)/CBS for the stationary points. The reaction path degeneracy and transition state chirality for each reaction was also incorporation into the partition functions. The inequivalent transition states were explicitly included in the sum in the numerator of eq. (3). The SCT tunneling coefficients, κ_i^{SCT}, were computed along the reaction pathway that was computed at the M11 level. The values of $\kappa_i^{SCT}(T = 298K)$ are shown in Table 4.

Table 4. Factors for the reaction path degeneracy (n), transition state chirality (m) and small-curvature tunneling coefficient for HO_2 with PA(Tc) and PA(Tt) at T=298K which were used when determining the rate coefficients. R6[a] and R6[b] correspond to passing over different standpoints leading to the final products of $CH_3(CO)OH+CO_2+OH$. Here R6[a] corresponds to TS13 and R6[b] to TS14.

T=298K	n	m	κ^{SCT}
R1	3	2	51.11
R2	1	2	12603.35
R6[a]	1	2	27.90
R6[b]	1	2	148.79

The reactions R1, R2, and R6 were all found to have significant transmission coefficients at T=298K. The reactions proceed through very narrow barriers, i.e. the barrier frequencies were 2334.2i cm^{-1} 4896.9i cm^{-1}, and 1369.9i cm^{-1}(2245.8i cm^{-1}) for TS1, TS2, and TS13(TS14). It is interesting that the barrier TS14 is significantly narrower than its conformational partner TS13. Although the transmission through TS14 is higher than that through TS13, the difference in the barrier heights still strongly favors the TS13 route. The values for the rate coefficients are presented in Table 5 and a graph showing the effective rate constant with and without tunneling (NT) are presented in Figure 10.

Table 5. Rate coefficient for reactions R1, R2, and R6 as well as the effective rate constant of $PA+HO_2$ studied calculated with the CCSD(T)/CBS energetics at T=200K, 250K, 298K and 350K in cm^3 molecule^{-1} s^{-1}.

$T(K)$	k_{R1}	k_{R2}	k_{R6}	k_{eff}
200	1.82x10^{-32}	3.64x10^{-40}	1.20x10^{-20}	1.20x10^{-20}
250	2.87x10^{-29}	1.35x10^{-35}	1.69x10^{-20}	1.69x10^{-20}
298	4.11x10^{-27}	1.43x10^{-32}	2.88x10^{-20}	2.88x10^{-20}
350	2.26x10^{-25}	3.73x10^{-30}	5.65 x10^{-20}	5.65 x10^{-20}

It is apparent that k_{R6} is totally dominant in the reaction process. A non-linear least squares fit was generated from the effective rate constant and is presented in Table 6.

Table 6. Exponential Ahrenius fit of the effective rate coefficient for PA+HO_2 using CCSD(T)/CBS. These are fit with the form $k = A_1 \ T^{n_1} \ e^{-\frac{B_1}{T}}$. Units for this fit are molecule cm^3 s^{-1} and Kelvin.

A_1	n_1	B_1
1.318×10^{-49}	10.65	-2051.812

A graph showing the effective rate constant calculated with and without the small-curvature tunneling correction (NT) is presented in Fig. 10.

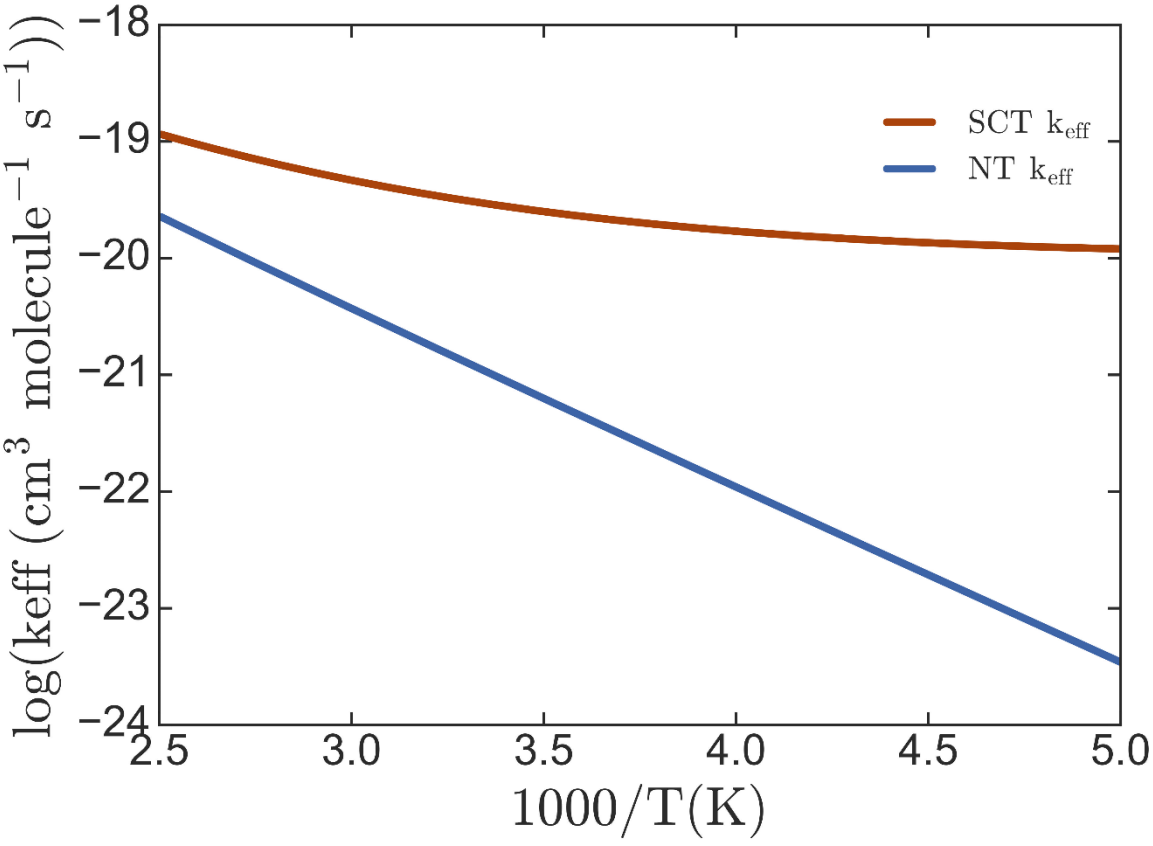

Figure 10. Effective rate constant, including R1, R2, and R6, for the reaction PA+HO_2 calculated over the range of 200 to 400 K. This figure includes both the small-curvature tunneling corrected rate constant (Orange), as well as rate constants neglecting any tunneling (Blue) to show the importance of tunneling at low temperatures.

Despite the catalytic effect that HO_2 plays on the reaction barriers with pyruvic acid, the effective overall rate constant is primarily determined by the lowest energy bottleneck of the sequential H-atom transfer reaction R6, via the bottleneck TS13. The reactions of R1 through R5, which involve hydrogen transfer isomerization or hydrogen abstraction by HO_2, do not contribute significantly to the overall rate constant. It is quite interesting to note that internal barriers to the concerted hydrogen exchange processes of R3-R5 are significantly lower than the previously observed unimolecular overtone induced isomerization reactions of PA.[41 42] The R6 reaction was found to be approximately six orders of magnitude larger than the upper limit rate constants of the R1 or R2 reactions at room temperature. As shown in Figure 10, the tunneling contribution calculated with the SCT method is quite significant even at room temperature with a SCT correction factor of 27.90 at 298K.

4. Conclusions

In this work the reaction of pyruvic acid with HO_2 was mechanistically and kinetically studied using *ab initio* quantum chemistry and TST. The reaction mechanisms were found to follow six distinct routes: abstraction (R1 and R2), exchange (R3-R5) or peroxy radical formation and isomerization (R6). It was found that HO_2 was able to mediate the hydrogen isomerization reactions and had a barrier lowering effect ranging from 7 to 25 kcal/mol. This provides a further example of the barrier lowering characteristics of double hydrogen exchange mechanism catalyzed by the HO_2 molecule. Despite this catalytic effect, these exchange reactions were very endothermic and unimportant in the consumption of PA, although they are interesting as examples of a chemical principle. We find reaction route R6 is kinetically dominant under ambient conditions. This multi-step pathway involves the formation of a peroxy species through hydrogen transfer process from the HO_2 moiety, followed by a second hydrogen transfer from the acid group. For this process to occur, the intermediate is required to undergo conformational change. Since the barrier for this isomerization process is low, we assume that the intermediates lie in an equilibrium distribution and the multiconformational adaptation of TST developed by Truhlar and coworkers[59 58] can be applied. We note that a mechanism similar to reaction R6 was previously proposed by da Silva.[7] The TST rate coefficient for R6 was found to be orders of magnitude larger than that for all other reactions at room temperature. The tunneling coefficient for R6 was quite important and was

found to increase the rate coefficient by a factor of 27.9 at room temperature. It is highly possible that other similar reactions may proceed by the da Silva mechanism.

In light of the results presented, it seems unlikely that the PA+HO_2 reaction has a major impact on the chemical consumption of PA in the atmosphere. The much faster rate for the PA+OH reaction would seem to more than compensate for the lower relative concentration of atmospheric OH versus HO_2. Thus, reactions with OH should dominate in the troposphere. Furthermore, as a sink for atmospheric PA, HOx reactions with PA are collectively much slower than the consumption of PA via solar photolysis during daytime. The reaction of pyruvic acid with HO_2 may still play some role as a potential source for OH radicals under certain atmospheric conditions, such as environments free of NOx or at nighttime when direct photolysis would not be operative. Under such conditions there are large HO_2/OH mixing ratios. This suggests that the potential conversion of HO_2 to OH via various atmospheric VOC's would seem to be worthy of further investigation.

Supporting Information for Publication

The Supporting Information is available free of charge at https://pubs.acs.org/doi/xxxxxxx. The supporting information consists of the geometries, energies, and frequencies of the stationary points obtained from the quantum chemistry calculations and a description of the numerical methods.

Acknowledgements

This work was supported by the National Science Foundation through grant CHE 1664555. This work utilized the RMACC Summit supercomputer, which is supported by the National Science Foundation (awards ACI-1532235 and ACI-1532236), the University of Colorado Boulder, and Colorado State University. The Summit supercomputer is a joint effort of the University of Colorado Boulder and Colorado State University. JC would like to acknowledge the Zuckerman STEM Leadership program for their support. VV acknowledges funding for this work by the National Science Foundation grant no. CHE 1611107

References

[1] Sindelarova, K.; Granier, C.; Bouarar, I.; Guenther, A.; Tilmes, S.; Stavrakou, T.; Müller, J.-F.; Kuhn, U.; Stefani, P.; Knorr, W. Global Data Set of Biogenic VOC Emissions Calculated by the MEGAN Model over the Last 30 Years. *Atmospheric Chem. Phys.* **2014**, *14* (17), 9317–9341.

[2] Atkinson R., Baulch, D. L., Cox, R. A. Crowley, J. N., Hampson, R. F., Hynes, R. G., Jenkin, M. E., Rossi, M. J., Troe, J., and IUPAC Subcommittee, Evaluated kinetic and photochemical data for atmospheric chemistry: Volume II – gas phase reactions of organic species, *Atmos. Chem. Phys.* **2006**, 6, 3625–4055.

[3] Karl, M., Dorn, H. P., Holland, F., Koppman, R., Poppe, D., Rupp, L., Schaub, A., Wahner, A. Product study of the reaction of OH radicals with isoprene in the atmosphere simulation chamber SAPHIR, *J. Atmos. Chem*. **2006**, 55 (2) 167-187.

[4] Atkinson, R., Kinetic of the gas-phase reactions of OH radicals with alkanes and cycloalkanes, *Atmospheric Chem. Phys.* **2003**, *3*, 2233-2307.

[5] Atkinson, R. Kinetics and Mechanisms of the Gas-Phase Reactions of the Hydroxyl Radical with Organic Compounds under Atmospheric Conditions. *Chem. Rev.* **1986**, *86* (1), 69–201.

[6] Heard, D. E.; Pilling, M. J. Measurement of OH and HO2 in the Troposphere. *Chem. Rev.* **2003**, *103* (12), 5163–5198.

[7] da Silva, G. Kinetics and Mechanism of the Glyoxal + HO_2 Reaction: Conversion of HO_2 to OH by Carbonyls. *J. Phys. Chem. A* **2011**, *115* (3), 291–297.

[8] Atkinson, R. Kinetics and Mechanisms of the Gas-Phase Reactions of the Hydroxyl Radical with Organic Compounds under Atmospheric Conditions. *Chem. Rev.* **1986**, *86* (1), 69–201.

[9] Atkinson, R.; Baulch, D. L.; Cox, R. A.; Crowley, J. N.; Hampson, R. F.; Hynes, R. G.; Jenkin, M. E.; Rossi, M. J.; Troe, J.; Subcommittee, I. Evaluated Kinetic and Photochemical Data for Atmospheric Chemistry: Volume II–Gas Phase Reactions of Organic Species. *Atmospheric Chem. Phys.* **2006**, *6* (11), 3625–4055.

[10] Moortgat, G. K. Important Photochemical Processes in the Atmosphere. *Pure Appl. Chem.* **2001**, *73* (3), 487–490.

[11] Epstein, S. A.; Nizkorodov, S. A. A Comparison of the Chemical Sinks of Atmospheric Organics in the Gas and Aqueous Phase. *Atmospheric Chem. Phys.* **2012**, *12* (17), 8205–8222.

[12] Sander, S. P.; Abbatt, J.; Barker, J. R.; Burkholder, J. B.; Friedl, R. R.; Golden, D. M.; Huie, R. E.; Kolb, C. E.; Kurylo, M. J.; Moortgat, G. K. Chemical Kinetics and Photochemical Data for Use in Atmospheric Studies, Evaluation No. 17. *JPL Publication* **2006**, No. 10–6.

[13] Crounse, J. D.; Nielsen, L. B.; Jørgensen, S.; Kjaergaard, H. G.; Wennberg, P. O. Autoxidation of Organic Compounds in the Atmosphere. *J. Phys. Chem. Lett.* **2013**, *4* (20), 3513–3520..

[14] Møller, K. H.; Bates, K. H.; Kjaergaard, H. G. The Importance of Peroxy Radical Hydrogen-Shift Reactions in Atmospheric Isoprene Oxidation. *J. Phys. Chem. A* **2019**, *123* (4), 920–932.

[15] Møller, K. H.; Otkjær, R. V.; Hyttinen, N.; Kurtén, T.; Kjaergaard, H. G. Cost-Effective Implementation of Multiconformer Transition State Theory for Peroxy Radical Hydrogen Shift Reactions. *J. Phys. Chem. A* **2016**, *120* (51), 10072–10087.

[16] Praske, E.; Otkjær, R. V.; Crounse, J. D.; Hethcox, J. C.; Stoltz, B. M.; Kjaergaard, H. G.; Wennberg, P. O. Atmospheric Autoxidation Is Increasingly Important in Urban and Suburban North America. *Proc. Natl. Acad. Sci. U.S.A* **2018**, *115* (1), 64–69.

[17] Veres, P. R.; Roberts, J. M.; Cochran, A. K.; Gilman, J. B.; Kuster, W. C.; Holloway, J. S.; Graus, M.; Flynn, J.; Lefer, B.; Warneke, C. Evidence of Rapid Production of Organic Acids in an Urban Air Mass. *Geophys. Res. Lett.* **2011**, *38* (17).

[18] Nguyen, T. B.; Bateman, A. P.; Bones, D. L.; Nizkorodov, S. A.; Laskin, J.; Laskin, A. High-Resolution Mass Spectrometry Analysis of Secondary Organic Aerosol Generated by Ozonolysis of Isoprene. *Atmos. Environ.* **2010**, *44* (8), 1032–1042.

[19] Carlton, A. G.; Turpin, B. J.; Lim, H.-J.; Altieri, K. E.; Seitzinger, S. Link between Isoprene and Secondary Organic Aerosol (SOA): Pyruvic Acid Oxidation Yields Low Volatility Organic Acids in Clouds. *Geophys. Res. Lett.* **2006**, *33* (6).

[20] Chebbi, A.; Carlier, P. Carboxylic Acids in the Troposphere, Occurrence, Sources, and Sinks: A Review. *Atmos. Environ.* **1996**, *30* (24), 4233–4249.

[21] Veres, P.; Roberts, J. M.; Burling, I. R.; Warneke, C.; de Gouw, J.; Yokelson, R. J. Measurements of Gas-phase Inorganic and Organic Acids from Biomass Fires by Negative-ion

Proton-transfer Chemical-ionization Mass Spectrometry. *J. Geophys. Res. Atmos.* **2010**, *115* (D23).

[22] Andreae, M. O.; Talbot, R. W.; Li, S.-M. Atmospheric Measurements of Pyruvic and Formic Acid. *J. Geophys. Res. Atmos.* **1987**, *92* (D6), 6635–6641.

[23] Talbot, R. W.; Mosher, B. W.; Heikes, B. G.; Jacob, D. J.; Munger, J. W.; Daube, B. C.; Keene, W. C.; Maben, J. R.; Artz, R. S. Carboxylic Acids in the Rural Continental Atmosphere over the Eastern United States during the Shenandoah Cloud and Photochemistry Experiment. *J. Geophys. Res. Atmos.* **1995**, *100* (D5), 9335–9343.

[24] Grosjean, D.; Williams, E. L.; Grosjean, E. Atmospheric Chemistry of Isoprene and of Its Carbonyl Products. *Environ. Sci. Technol.* **1993**, *27* (5), 830–840.

[25] Grosjean, D.; Williams, E. L.; Grosjean, E. Atmospheric Chemistry of Isoprene and of Its Carbonyl Products. *Environ. Sci. Technol.* **1993**, *27* (5), 830–840.

[26] Vaida, V. Sunlight Initiated Atmospheric Photochemical Reactions. *Int. J. Photoenergy* **2005**, *7* (2), 61–70.

[27] Vaida, V. Spectroscopy of Photoreactive Systems: Implications for Atmospheric Chemistry. *J. Phys. Chem. A* **2008**, *113* (1), 5–18.

[28] Rapf, R. J.; Vaida, V. Sunlight as an Energetic Driver in the Synthesis of Molecules Necessary for Life. *Phys. Chem. Chem. Phys.* **2016**, *18* (30), 20067–20084.

[29] Griffith, E. C.; Tuck, A. F.; Vaida, V. Ocean–Atmosphere Interactions in the Emergence of Complexity in Simple Chemical Systems. *Acc. Chem. Res.* **2012**, *45* (12), 2106–2113.

[30] Blair, S. L.; Reed Harris A. E.; Frandsen B. N.; Kjaergaard H. G.; Pangui E.; Cazaunau M.; Doussin J. -F.; Vaida V., Conformer-Specific Photolysis of Pyruvic Acid and the effect of Water" *J. Phys. Chem A,* **124(**7), 1240-1252 (2020) DOI:10.1021/acs.jpca.9b10613

[31] Reed Harris, A. E.; Doussin, J.-F.; Carpenter, B. K.; Vaida, V. Gas-Phase Photolysis of Pyruvic Acid: The Effect of Pressure on Reaction Rates and Products. *J. Phys. Chem A.* **2016**, *120* (51), 10123–10133.

[32] Vesley, G. F.; Leermakers, P. A. The Photochemistry of α-Keto Acids and α-Keto Esters. III. Photolysis of Pyruvic Acid in the Vapor Phase. *J. Phys. Chem.* **1964**, *68* (8), 2364–2366.

[33] Dhanya, S.; Maity, D. K.; Upadhyaya, H. P.; Kumar, A.; Naik, P. D.; Saini, R. D. Dynamics of OH Formation in Photodissociation of Pyruvic Acid at 193 Nm. *J. Chem. Phys.* **2003**, *118* (22), 10093–10100.

[34] O'Neill, J. A.; Kreutz, T. G.; Flynn, G. W. IR Diode Laser Study of Vibrational Energy Distribution in CO2 Produced by UV Excimer Laser Photofragmentation of Pyruvic Acid. *J. Chem. Phys.* **1987**, *87* (8), 4598–4605.

[35] Berges, M. G.; Warneck, P. Product Quantum Yields for the 350 Nm Photodecomposition of Pyruvic Acid in Air. *Berichte der Bunsengesellschaft für physikalische Chemie* **1992**, *96* (3), 413–416.

[36] Back, R. A.; Yamamoto, S. The Gas-Phase Photochemistry and Thermal Decomposition of Glyoxylic Acid. *Can. J. Chem.* **1985**, *63* (2), 542–548.

[37] Saito, K.; Sasaki, G.; Okada, K.; Tanaka, S. Unimolecular Decomposition of Pyruvic Acid: An Experimental and Theoretical Study. *J. Phys. Chem.* **1994**, *98* (14), 3756–3761.

[38] Chang, X.-P.; Fang, Q.; Cui, G. Mechanistic Photodecarboxylation of Pyruvic Acid: Excited-State Proton Transfer and Three-State Intersection. *J. Chem. Phys.* **2014**, *141* (15), 154311.

[39] Kakkar, R.; Pathak, M.; Radhika, N. P. A DFT Study of the Structures of Pyruvic Acid Isomers and Their Decarboxylation. *Org. Biomol. Chem.* **2006**, *4* (5), 886–895.

[40] Schreiner, P. R.; Reisenauer, H. P.; Ley, D.; Gerbig, D.; Wu, C.-H.; Allen, W. D. Methylhydroxycarbene: Tunneling Control of a Chemical Reaction. *Science* **2011**, *332* (6035), 1300–1303.

[41] Takahashi, K.; Plath, K. L.; Skodje, R. T.; Vaida, V. Dynamics of Vibrational Overtone Excited Pyruvic Acid in the Gas Phase: Line Broadening through Hydrogen-Atom Chattering. *J. Phys. Chem. A* **2008**, *112* (32), 7321–7331.

[42] da Silva, G. Decomposition of Pyruvic Acid on the Ground-State Potential Energy Surface. *J. Phys. Chem. A* **2015**, *120* (2), 276–283.

[43] Reed Harris, A. E.; Ervens, B.; Shoemaker, R. K.; Kroll, J. A.; Rapf, R. J.; Griffith, E. C.; Monod, A.; Vaida, V. Photochemical Kinetics of Pyruvic Acid in Aqueous Solution. *J. Phys. Chem A.* **2014**, *118* (37), 8505–8516.

[44] Reed Harris, A. E.; Pajunoja, A.; Cazaunau, M.; Gratien, A.; Pangui, E.; Monod, A.; Griffith, E. C.; Virtanen, A.; Doussin, J.-F.; Vaida, V. Multiphase Photochemistry of Pyruvic Acid under Atmospheric Conditions. *J. Phys. Chem. A* **2017**, *121* (18), 3327–3339.

[45] Reed Harris, A. E.; Cazaunau, M.; Gratien, A.; Pangui, E.; Doussin, J.-F.; Vaida, V. Atmospheric Simulation Chamber Studies of the Gas-Phase Photolysis of Pyruvic Acid. *J. Phys. Chem A.* **2017**, *121* (44), 8348–8358

[46] Guzman, M. I.; Colussi, A. J.; Hoffmann, M. R. Photoinduced Oligomerization of Aqueous Pyruvic Acid. *J. Phys. Chem. A* **2006**, *110* (10), 3619–3626.

[47] Griffith, E. C.; Carpenter, B. K.; Shoemaker, R. K.; Vaida, V. Photochemistry of Aqueous Pyruvic Acid. *Proc. Natl. Acad. Sci. U.S.A* **2013**, *110* (29), 11714–11719.

[48] Samanta, B. R., Fernando, R. Roesch, D., Reisler, H., Osborn, D. L. Looking at the bigger picture: Identifying the photoproducts of pyruvic acid at 193 nm. J. Chem. Phys. 2020 153 (7) 074307.

[49] Sutradhar, S., Samanta, B. R., Fernando, R., Reisler, H. Spectroscopy and Two-Photon Dissociation of Jet-Cooled Pyruvic Acid, *J. Phys. Chem. A* **2019** *123*, 28, 5906–5917.

[50] Samanta, B. R., Sutradhar, S. Fernando, R., Krylov, A.I . Reisler, H. Electronic Structure and Rydberg-Core Interactions in Hydroxycarbene and Methylhydroxycarbene. *J. Phys. Chem. A* **2018**, *122* (30), 6176-6182.

[51] Mellouki, A.; Mu, Y. On the Atmospheric Degradation of Pyruvic Acid in the Gas Phase. *J. Photochem. Photobiol. A : Chemistry* **2003**, *157* (2–3), 295–300.

[52] Church, J. R.; Vaida, V.; Skodje, R. T. Gas-Phase Reaction Kinetics of Pyruvic Acid with OH Radicals: The Role of Tunneling, Complex Formation, and Conformational Structure. *J. Phys. Chem. A* **2020**, *124* (5), 790–800. https://doi.org/10.1021/acs.jpca.9b09638.

[53] Church, J. R.; Skodje, R. T. Double Hydrogen-Atom Exchange Reactions of HX (X= F, Cl, Br, I) with HO_2. *J. Phys. Chem. A* **2018**, *122* (24), 5251–5260.

[54] Church, J. R.; Skodje, R. T. Reaction Kinetics of HBr with HO_2: A New Channel for Isotope Scrambling Reactions. *J. Phys. Chem. A* **2016**, *120* (43), 8503–8511.

[55] Karton, A. Inorganic Acid-Catalyzed Tautomerization of Vinyl Alcohol to Acetaldehyde. *Chem. Phys. Lett* **2014**, *592*, 330–333.

[56] Bao, J. L.; Meana-Pañeda, R.; Truhlar, D. G. Multi-Path Variational Transition State Theory for Chiral Molecules: The Site-Dependent Kinetics for Abstraction of Hydrogen from 2-Butanol by Hydroperoxyl Radical, Analysis of Hydrogen Bonding in the Transition State, and Dramatic Temperature Dependence of the Activation Energy. *Chem. Sci.* **2015**, *6* (10), 5866–5881. https://doi.org/10.1039/c5sc01848j.

[57] Vereecken, L.; Peeters, J. The 1,5-Shift in 1-Butoxy: A Case Study in the Rigorous Implementation of Transition State Theory for a Multirotamer System. *J. Chem. Phys.* **2003**, *119* (10), 5159–5170. https://doi.org/10.1063/1.1597479.

[58] Zheng, J.; Truhlar, D. G. Multi-Path Variational Transition State Theory for Chemical Reaction Rates of Complex Polyatomic Species: Ethanol+ OH Reactions. *Faraday Discuss.* **2012**, *157*, 59–88.

[59] Yu, T.; Zheng, J.; Truhlar, D. G. Multipath Variational Transition State Theory: Rate Constant of the 1, 4-Hydrogen Shift Isomerization of the 2-Cyclohexylethyl Radical. *J. Phys. Chem. A* **2011**, *116* (1), 297–308.

[60] Liu, Y. P.; Lynch, G. C.; Truong, T. N.; Lu, D. H.; Truhlar, D. G.; Garrett, B. C. Molecular Modeling of the Kinetic Isotope Effect for the [1,5]-Sigmatropic Rearrangement of Cis-1,3-Pentadiene. *J. Am. Chem. Soc.* **1993**, *115* (6), 2408–2415.

[61] Skodje, R. T.; Truhlar, D. G.; Garrett, B. C. A General Small Curvature Approximation for Transition-State-Theory Transmission Coefficients, *J. Phys. Chem.* **1981**, 85, 3019-3023.

[62] Skodje, R. T., Truhlar, D. G., Garrett B. C. Adiabatic Models for Reactive Scattering, *J. Chem Phys.* **1982** *77,* 5955-5975.

[63] Dunning, T. H. Gaussian Basis Sets for Use in Correlated Molecular Calculations. I. The Atoms Boron through Neon and Hydrogen. *J. Chem. Phys.* **1989**, *90* (2), 1007–1023. https://doi.org/10.1063/1.456153.

[64] Peverati, R.; Truhlar, D. G. Performance of the M11 and M11-L Density Functionals for Calculations of Electronic Excitation Energies by Adiabatic Time-Dependent Density Functional

Theory. *Phys. Chem. Chem. Phys.* **2012**, *14* (32), 11363–11370. https://doi.org/10.1039/c2cp41295k.

[65] Hratchian, H. P.; Kraka, E. Improved Predictor–Corrector Integrators For Evaluating Reaction Path Curvature. *J. Chem. Theory Comput.* **2013**, *9* (3), 1481–1488.

[66] Hratchian, H. P. Using Efficient Predictor-Corrector Reaction Path Integrators for Studies Involving Projected Frequencies. *J. Chem. Theory Comput.* **2012**, *8* (12), 5013–5019.

[67] Hratchian, H. P.; Schlegel, H. B. Using Hessian Updating to Increase the Efficiency of a Hessian Based Predictor-Corrector Reaction Path Following Method. *J. Chem. Theory Comput.* **2005**, *1* (1), 61–69.

[68] Gonzalez, C.; Schlegel, H. B. Reaction Path Following in Mass-Weighted Internal Coordinates. *J. Phys. Chem.* **1990**, *94* (14), 5523–5527.

[69] Qiu, Y. Pushing the Ab Initio Limits for the Accurate Characterization of Small Molecular Systems, University of Georgia, 2015.

[70] Schmidt, M. W.; Baldridge, K. K.; Boatz, J. A.; Elbert, S. T.; Gordon, M. S.; Jensen, J. H.; Koseki, S.; Matsunaga, N.; Nguyen, K. A.; Su, S. General atomic and molecular electronic structure system *J. Comput. Chem.* **1993**, 14, 1347– 1363.

[71] Gaussian 16, Revision B.01, M. J. Frisch, G. W. Trucks, H. B. Schlegel, G. E. Scuseria, M. A. Robb, J. R. Cheeseman, G. Scalmani, V. Barone, G. A. Petersson, H. Nakatsuji, X. Li, M. Caricato, A. V. Marenich, J. Bloino, B. G. Janesko, R. Gomperts, B. Mennucci, H. P. Hratchian, J. V. Ortiz, A. F. Izmaylov, J. L. Sonnenberg, D. Williams-Young, F. Ding, F. Lipparini, F. Egidi, J. Goings, B. Peng, A. Petrone, T. Henderson, D. Ranasinghe, V. G. Zakrzewski, J. Gao, N. Rega, G. Zheng, W. Liang, M. Hada, M. Ehara, K. Toyota, R. Fukuda, J. Hasegawa, M. Ishida, T. Nakajima, Y. Honda, O. Kitao, H. Nakai, T. Vreven, K. Throssell, J. A. Montgomery, Jr., J. E. Peralta, F. Ogliaro, M. J. Bearpark, J. J. Heyd, E. N. Brothers, K. N. Kudin, V. N. Staroverov, T. A. Keith, R. Kobayashi, J. Normand, K. Raghavachari, A. P. Rendell, J. C. Burant, S. S. Iyengar, J. Tomasi, M. Cossi, J. M. Millam, M. Klene, C. Adamo, R. Cammi, J. W. Ochterski, R. L. Martin, K. Morokuma, O. Farkas, J. B. Foresman, and D. J. Fox, Gaussian, Inc., Wallingford CT, **2016**.

TOC